Journal of Structural Geology 33 (2011) 1509–1522

Contents lists available at ScienceDirect

Journal of Structural Geology

journal homepage: www.elsevier.com/locate/jsg

Vein development during folding in the upper brittle crust: The case of tourmaline-rich veins of eastern Elba Island, northern Tyrrhenian Sea, Italy

Francesco Mazzarini [a,*], Giovanni Musumeci [a,b], Alexander R. Cruden [c]

[a] Istituto Nazionale di Geofisica e Vulcanologia, Pisa, Italy
[b] Dipartimento di Scienze della Terra, Università di Pisa, Italy
[c] School of Geosciences, Monash University, Melbourne, Australia

ARTICLE INFO

Article history:
Received 23 November 2010
Received in revised form
22 June 2011
Accepted 17 July 2011
Available online 29 July 2011

Keywords:
Thermal aureole
Upper crust
Deformation
Fluid circulation
Northern Apennines
Elba Island

ABSTRACT

Detailed structural analysis of tourmaline-rich veins hosted in the contact aureole of the ~6 Ma Porto Azzurro granite in southeastern Elba Island, northern Tyrrhenian Sea is presented. Using geometric features of the veins, the physical conditions at the time of vein formation are estimated, namely the stress ratio ($\Phi = (\sigma_2 - \sigma_3)/(\sigma_1 - \sigma_3)$), driving stress ratio ($R' = (P_f - \sigma_3)/(\sigma_1 - \sigma_3)$) and fluid overpressure ($\Delta P_o = P_f - \sigma_3$). Two vein sets (A veins and B veins) have been recognized based on orientation and thickness distributions and infilling material. Analysis of vein pole distributions indicates $\Phi = 0.57$ and $R' = 0.24$ for the A veins and $\Phi = 0.58$ and $R' = 0.47$ for the B veins, and fluid pressures less than the intermediate stress magnitude. Analysis of geometric features of the veins gives estimated fluid overpressures of between ~16 MPa (A veins) and ~32 MPa (B veins). We propose a model for the tectonic environment of vein development, in which formation of secondary permeability in the deforming thermal aureole of the Porto Azzurro pluton was controlled by ongoing development of fracture systems in the hinge zone of a regional NNW–SSE trending fold that favored transport and localization of hydrothermal fluids.

1. Introduction

Mutual relationships between deformation and metamorphic processes play a major role in controlling fluid circulation in the crust due to the development of secondary permeability at the microscale (microcracks) and/or mesoscale, allowing fluid migration through host rocks, often over large distances, and via different hydraulic pathways (Etheridge et al., 1983; McCaig, 1988; Oliver et al., 1990; Oliver, 1996). Thermal aureoles of intrusions are common sites of intense circulation of fluids released by crystallizing magmas (e.g., Norton and Knight, 1977; Nabelek et al., 1984; Harris et al., 2003). Depending on the magma temperature and host-rock composition, once an intrusion releases late-magmatic fluids, metasomatism and vein formation (e.g., Shearer et al., 1984; Woodford et al., 2001; Dini et al., 2008) or fluid enhanced incongruent biotite melting of host rocks (e.g., Harris et al., 2003) may occur.

In the northern Apennines, Miocene to Present magmatic activity is characterized by voluminous upper-crustal intrusions and scant volcanism (Tuscan Magmatic Province; Serri et al., 1993; Rosenbaum et al., 2008) that resulted in intense convective hydrothermal circulation recorded by hydrothermal mineralization, ore deposits and active geothermal systems (e.g., Larderello-Travale and Mt. Amiata geothermal fields; Tanelli, 1983; Gianelli et al., 1997a; Dini et al., 2005; Bertini et al., 2006).

The Larderello-Travale geothermal field is dominated by meteoric fluids that circulate within an upper sedimentary-rock sequence and a deep (4–6 km), high-temperature hydrothermal reservoir of exsolved magmatic fluids that circulate in a contact aureole immediately above a recently-emplaced intrusion (Gianelli et al., 1997b; Ruggieri et al., 1999, 2004; Ruggieri and Gianelli, 1999; Carella et al., 2000; Musumeci et al., 2002; Bertini et al., 2006; Casini et al., 2010). Recent studies of the deepest portion of the geothermal field from high-resolution 3D seismic data indicate that circulation of high-temperature fluids in the contact aureole is mainly controlled by fractures (Bertini et al., 2006; Casini et al., 2010). The heat source for the formation of the contact aureole in the Larderello-Travale geothermal field is supplied by multiple, shallow crustal-level granitic intrusions whose ages range between 1 and 4 Ma (Gianelli et al., 1997a; Dini et al., 2005; Franceschini, 1994, 1998).

In Eastern Elba Island, about 70 km south-west of Larderello, interactions between late-magmatic fluids and a contact aureole

* Corresponding author. Tel.: +39 508311956.
E-mail address: mazzarini@pi.ingv.it (F. Mazzarini).

0191-8141/$ – see front matter © 2011 Elsevier Ltd. All rights reserved.
doi:10.1016/j.jsg.2011.07.001

are recorded above the shallow, late Miocene (5.9 Ma), Porto Azzurro pluton (Dini et al., 2008). Late-magmatic fluids released into the hornfelsic contact aureole of the Porto Azzurro pluton produced boron-rich (tourmaline) veins and metasomatic bodies (Dini et al., 2008). Eastern Elba Island may therefore represent an exhumed equivalent of the deepest part of the Larderello-Travale geothermal field (Bertini et al., 2006; Dini et al., 2008), and hence represents a suitable natural laboratory to study the development of secondary permeability in a contact aureole.

In order to understand how fluids circulate within contact aureoles it is important to characterize the state of stress, fluid overpressure and formation depth of high-temperature hydrothermal veins, as well as the tectonic environment in which they were emplaced. Here we present a detailed structural analysis of tourmaline-rich veins hosted in the contact aureole of the ~6.0 Ma old Porto Azzurro granite pluton (Maineri et al., 2003; Musumeci et al., 2011). Using geometric features of the veins (attitude, thickness and aspect ratio) we estimate the physical conditions at the time of vein formation. Finally, a conceptual model for the tectonic environment in which the veins developed is proposed on the basis of detailed field mapping of southeastern Elba Island and structural analysis of the veins and their host rock. We propose that the veins and associated secondary permeability formed due to the development of fracture systems in the hinge zone of a growing anticline thus favoring transport and localization of fluids in the deforming thermal aureole.

2. Theoretical background

2.1. Physical conditions of vein formation

Brittle-rock failure depends on the coefficient of internal friction and the balance between differential stress ($\sigma_1 - \sigma_3$) and rock tensile strength T_o (Secor, 1965; Brace, 1978; Byerlee, 1978). The type of failure affecting an intact rock mass greatly depends on the fluid pressure (P_f), which controls the principal effective stresses (Sibson, 2000 and references therein) σ_i',

$$\sigma_1' = \left(\sigma_1 - P_f\right) > \sigma_2' = \left(\sigma_2 - P_f\right) > \sigma_3' = \left(\sigma_3 - P_f\right) \quad (1)$$

where σ_i ($i = 1,2,3$) are the principal stresses.

The ratio of pore-fluid pressure to lithostatic pressure ($\sigma_v = \rho g z$) is defined as:

$$\lambda = \frac{P_f}{\rho g z} \quad (2)$$

where ρ is the rock density, g is the gravitational acceleration and z is the depth.

Hydrostatic fluid pressure is attained when pores and fractures are interconnected up to the water table, which is assumed to reach the ground surface ($\lambda \sim 0.4$). Supra-hydrostatic fluid pressure conditions are defined by $0.4 < \lambda < 1.0$, while supra-lithostatic conditions are defined by $\lambda > 1.0$ (Sibson, 2000).

Several parameters related to both the effective-stress field and fluid pressure can be derived through analysis of the geometry of fluid filled cracks, including their orientations and aspect ratios (i.e., veins or dikes; e.g., Baer et al., 1994; Jolly and Sanderson, 1997; Gudmundsson, 1999; André et al., 2001; McKeagney et al., 2004; Mazzarini and Isola, 2007; Mazzarini and Musumeci, 2008; Mazzarini et al., 2010).

The stress ratio (Φ) and the driving stress ratio (R') are defined in terms of the principal stresses and fluid pressure (Baer et al., 1994; Jolly and Sanderson, 1997):

$$\Phi = \frac{(\sigma_2 - \sigma_3)}{(\sigma_1 - \sigma_3)} \quad (3)$$

and

$$R' = \frac{\left(P_f - \sigma_3\right)}{(\sigma_1 - \sigma_3)} \quad (4)$$

The stress ratio ranges from 0 to 1 and describes the Mohr circle configuration (Angelier, 1984; Baer et al., 1994; Orife and Lisle, 2003). The driving stress ratio (Baer et al., 1994) varies from −1 (no opening of fractures) to 1 (re-opening of pre-existing fractures), and describes the equilibrium between P_f and the minimum and maximum stresses.

The orientation distribution of poles to veins can be used to infer the stress ratio and the driving stress ratio from (Baer et al., 1994; Jolly and Sanderson, 1997):

$$\Phi = \frac{(1 + \cos 2\theta_2)}{(1 + \cos 2\theta_1)} \quad Pf > \sigma_2 \quad (5)$$

$$\Phi = 1 - \left[\frac{(1 - \cos 2\theta_2)}{(1 - \cos 2\theta_3)}\right] \quad Pf > \sigma_2 \quad (6)$$

and

$$R' = \frac{(1 + \cos 2\theta_2)}{2} \quad (7)$$

where, on lower-hemisphere stereographic projections, θ_1 is the angle between σ_2 and the border of the pole distribution of fluid filled cracks (in this case veins) in the σ_2–σ_3 plane, θ_2 is the angle between σ_1 and the border of the pole distribution in the σ_1–σ_3 plane, and θ_3 is the angle between σ_1 and the border of the pole distribution in the σ_1–σ_2 plane (Jolly and Sanderson, 1997). The orientations of the principal stress axes are derived from vein orientations by calculating the Bingham distribution (e.g., Press et al., 1986) of poles to veins, and then assigning each eigenvector to the appropriate principal stress.

The vein aspect ratio (W/L) is defined as the ratio between maximum vein aperture (W) and vein length (L). It can be used to derive static fluid overpressure (driving pressure) during vein formation, assuming that it is related linearly to fluid overpressure ($\Delta P_o = P_f - \sigma_3$) and the elastic rock properties (Gudmundsson, 1999 and references therein):

$$\frac{W}{L} = \frac{\Delta P_o 2(1 - \nu^2)}{E} \quad (8)$$

where ν and E are the host rock Poisson ratio and Young's modulus, respectively.

2.2. Thickness and spacing distribution of veins

Geometric features of veins such as thickness (W) and spacing (S) are typically characterized by scale invariance (e.g., Johnston and McCaffrey, 1996; McCaffrey and Johnston, 1996; Roberts et al., 1999; Gillespie et al., 1999; Bonnet et al., 2001) and are analyzed in terms of their cumulative frequency distribution:

$$N(>X) = cX^{-a} \quad (9)$$

where c is a normalization constant, X is a geometric feature of the veins (thickness or spacing) and a is the power-law (fractal) exponent. As rule of thumb, a size range of at least one order of magnitude and at least 50 samples is required for extracting reliable parameter estimates (Bonnet et al., 2001; Clauset et al., 2009).

Any distribution on a $\log(N(X))$ *vs* $\log(X)$ plot is described by the fractal exponent a and also by the maximum value of the distribution (X_{MAX}), derived by imposing $N(X) = 1$ in Eq. (9).

The following points should be considered when determining c and a: (1) the error associated with the resolution limit of measurement (truncation), and (2) the error resulting from values of the measured feature extending beyond the sampling window (censoring). The effect of truncation is to underestimate the contributions of measurements (e.g., thickness) below the resolution of the acquisition method (for example, veins with thickness less than 0.5 mm). The effect of censoring is to underestimate measurements extending beyond the sampling window (e.g., spacing greater than a few tens of meters). Comparison of theoretical maximum values of the distribution (L_{MAX}) with the maximum observed value can thus give an indication of the influence of censoring and truncation; the higher the difference between these values, the higher is the influence of undersampling.

The thickness distributions of veins have been described both by power-law and negative exponential laws (e.g., Johnston and McCaffrey, 1996; Gillespie et al., 1999; Roberts et al., 1999). A power-law distribution predicts the occurrence of a relatively large number of thick veins, whereas other distributions (e.g., negative exponential) have a characteristic size with a very low abundance of thicknesses above or below the scale of observations.

Vein thickness distribution has been used to infer the mechanism of vein growth (e.g., Clark et al., 1995; Roberts et al., 1999). Stratabound veins have thickness distributions that are generally negative exponential or log-normal, whereas non-stratabound veins commonly have a power-law thickness distribution (Gillespie et al., 1999). Clark et al. (1995) proposed that under conditions of constant vein nucleation, the time-averaged growth rate is proportional to the thickness, which is characterized by a power-law distribution. A negative exponential distribution for vein thicknesses is expected for a constant vein growth rate. Monecke et al. (2001) assumed that the fractal exponent $a(\alpha/\gamma)$ is function of the nucleation (α) to growth-rates (γ) ratio. High nucleation rates lead to a large fractal exponent (i.e., a distribution dominated by numerous thin veins), whereas very fast growth rates produce a low fractal exponent (i.e., a distribution dominated by thick veins). The formation of veins by hydrofracturing implies large fluid pressures (e.g., Hedenquist and Lowenstern, 1994) resulting in high nucleation rates and high vein densities that is reflected by low vein spacing.

The homogeneity of the distributions of vein thicknesses and their spacing is also analyzed using the coefficient of variation C_v, which is defined as the ratio between the standard deviation and the mean values of the analyzed distribution (Gillespie et al., 1999 and references therein). C_v describes the degree of clustering of the distribution. $C_v > 1$ indicates a clustering of events, $C_v = 1$ indicates a random or Poisson distribution of events, and $C_v < 1$ indicates an anti-clustering (a homogeneous distribution) of events.

3. Geological setting of Elba Island

The northern Apennines belt was formed by continental collision between the European margin and the Adria promontory after closure of the Ligurian-Piedmont oceanic domain (Boccaletti et al., 1971). The belt's architecture resulted from late Oligocene – early-middle Miocene (Burdigalian) eastward nappe stacking of tectonic units scraped off the Tethyan oceanic crust (Ligurian units) and the Adria continental margin (Tuscan Nappes and Tuscan Metamorphic Complex). Since the late Miocene, the inner portion (Tyrrhenian side) of the northern Apennines region has been the site of subduction-related calc-alkaline magmatism (Tuscan Magmatic Province; Serri et al., 1993; Rosenbaum et al., 2008) characterized by mainly intrusive rocks, which extend from the northern Tyrrhenian Sea (Capraia, Giglio, Montecristo and Elba islands) to the inner portion of the northern Apennines. The age of magmatism becomes younger toward the east, with ages ranging from 8.4 (Capraia and Elba islands) to 0.2 Ma (Mt. Amiata). This magmatism was coeval with the opening of the Tyrrhenian Sea as a back-arc basin as a consequence of slab roll-back of the westward subducting lithosphere of Adria (Rosenbaum and Lister, 2004; Malinverno and Ryan, 1986). Late Miocene and Pliocene crustal extension has been invoked by many authors to explain the occurrence of magmatism and Neogene sedimentary basins in the northern Apennines (Serri et al., 1993; Keller and Coward, 1996; Bartole, 1995; Jolivet et al., 1998; Bossio et al., 1998).

Elba Island is one of the westernmost portions of the northern Apennine belt, located in the northern Tyrrhenian Sea, close to the western side of Alpine belt of northern Corsica. The structural setting of Elba Island (Fig. 1a) consists of a stack of NE-verging tectonic units derived from both continental (Adrian) and oceanic (Ligurian) domains, intruded by late Miocene igneous rocks (Barberi et al., 1967; Keller and Coward, 1996; Pertusati et al., 1993; Bortolotti et al., 2001). Tectonic units are subdivided into two thrust complexes separated by a main thrust zone (Fig. 1). The upper complex is an imbricate fan of three thrust sheets made up of sedimentary and very low-grade metamorphic rocks. From the top to the bottom, the thrust sheets are: (i) the Cretaceous–Paleogene Flysch Unit, (ii) the Mesozoic Ligurian Unit (ophiolitic rocks and sedimentary cover), and (iii) the Tuscan nappe (Late Triassic-Jurassic carbonate and marly rocks).

The lower complex (Fig. 1a,b) consists of two metamorphic units comprising the Calamita and Ortano Units. The Calamita Unit is made up of medium and high metamorphic grade pelitic-psammitic hornfelses (Calamita Schists and Verrucano Fm), followed upward by medium metamorphic grade marble hornfels (Calanchiole Marble; Garfagnoli et al., 2005). The Ortano Unit is an imbricate fan of Paleozoic and Mesozoic thrust sheets, which, from bottom to top, consist of (i) low metamorphic grade metasandstone and metavolcanics (Ortano Porphyroid), (ii) dolomitic marble hornfels (Ortano Marble) and (iii) medium and high metamorphic grade pelitic and carbonate hornfelses (Acquadolce Unit; Pertusati et al., 1993).

According to Keller and Coward, (1996), Pertusati et al. (1993) and Bortolotti et al. (2001), the tectonic evolution of Elba Island can be summarized in two stages:

(i) An early stage of folding and nappe stacking developed under very low metamorphic grade in the upper complex and under low metamorphic grade in the lower complex. In the lower complex this regional tectonic–metamorphic event is recorded by polyphase deformation with synkinematic growth of an albite + muscovite + chlorite mineral assemblage (Garfagnoli et al., 2005), which is dated at 19 Ma in the Ortano Unit (Deino et al., 1992).

(ii) In the late stage (Late Miocene), multiple magma inputs, ranging in age from ca. 8 to 5.9 Ma, led to the emplacement in the Elba Island nappe stack and two large composite intrusive bodies, together with systems of leucogranitic sills and laccoliths (Dini et al., 2002). In particular, the Monte Capanne pluton in the west and the Porto Azzurro pluton in the east were emplaced in the upper complex and lower complex, respectively, accompanied by the formation of contact metamorphic aureoles that overprinted previous fabrics and low-grade metamorphic mineral assemblages (Bouillin, 1983; Duranti et al., 1992; Garfagnoli et al., 2005). The

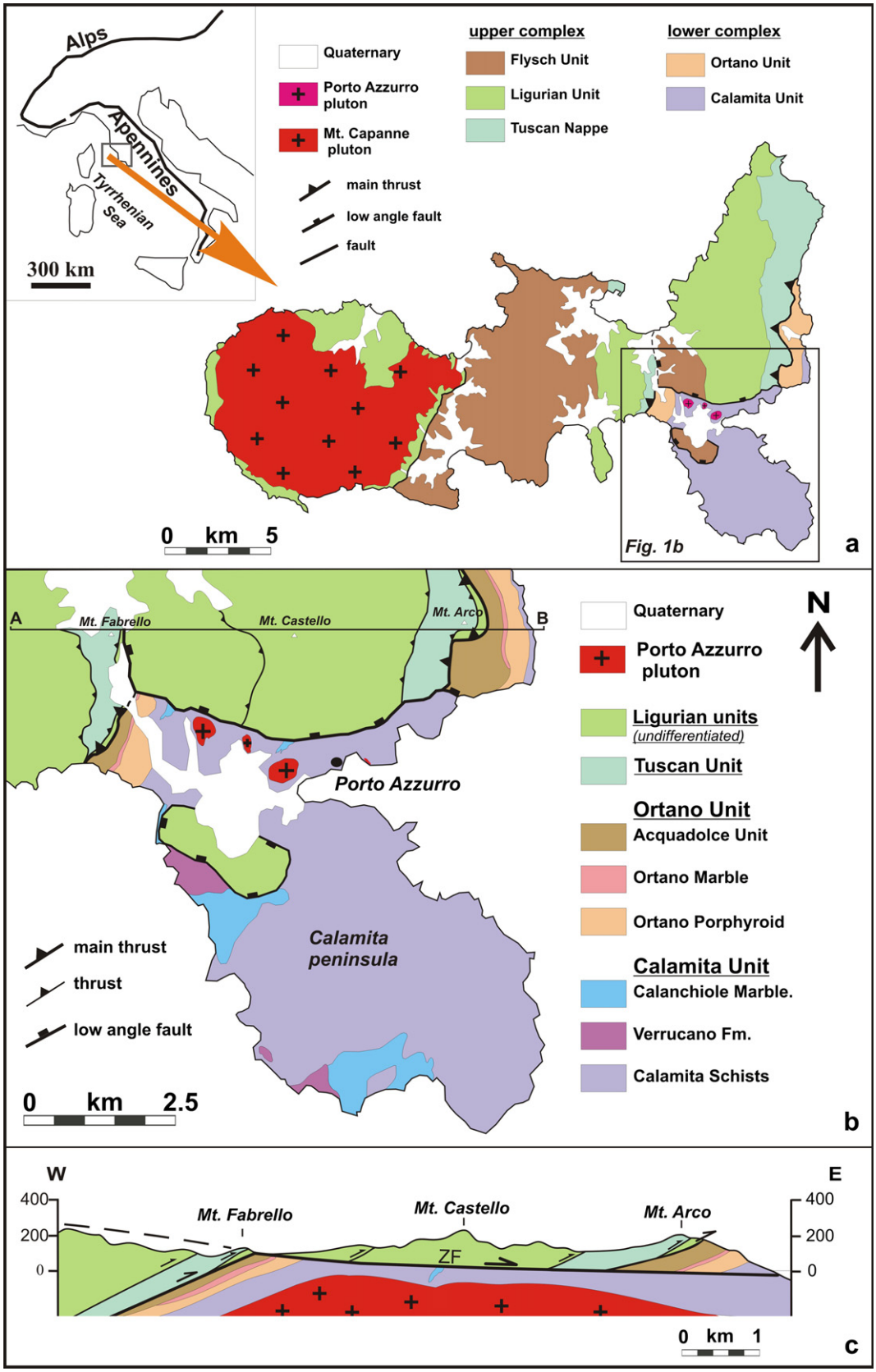

Fig. 1. a) Geological sketch map of Elba Island and location of the study area (after Dini et al., 2008; Mazzarini and Musumeci, 2008). b) Geological map of the southeastern Elba Island. c) Cross section showing the geometry of the thrust complex and eastward displacement along the Zuccale fault (ZF).

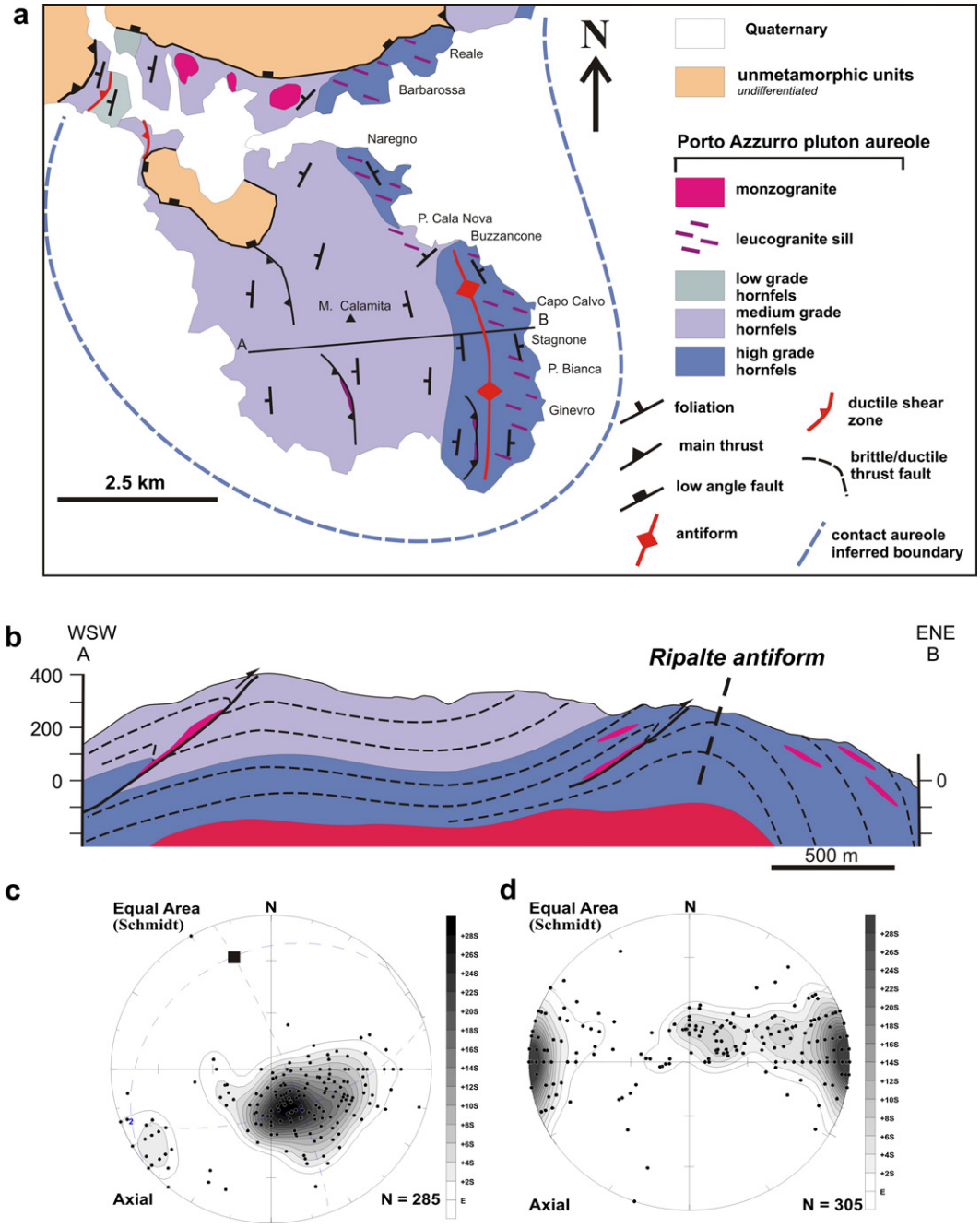

Fig. 2. a) Geology of the Calamita Peninsula showing the metamorphic grade distribution of hornfelses in the contact aureole of the Porto Azzurro pluton. b) Cross section of the Calamita peninsula showing the geometry of Ripalte antiform. c) Equal-area lower-hemisphere projection of poles to foliations within the Calamita Schist; large black square is the pole to the best fit great circle (342°/24°). d) Equal-area lower-hemisphere projection of poles to tourmaline veins in the Calamita Peninsula.

emplacement of intrusive bodies was followed by development of fault zones affecting the contact aureoles and the entire thrust system. These late structures have been ascribed to: (i) the collapse of the orogenic nappe pile during igneous intrusion (Pertusati et al., 1993; Garfagnoli et al., 2005), and (ii) crustal extension linked to the opening of the Tyrrhenian Sea (Keller and Coward, 1996; Collettini et al., 2006).

Within this framework, the Zuccale Fault (ZF; Fig. 1b, c) has been interpreted as an east-dipping low-angle fault (<10°) that crosscuts the nappe pile with eastward displacement of the hanging wall units from central to eastern Elba Island (Keller and Coward, 1996; Pertusati et al., 1993; Collettini et al., 2006). The geometry of and amount of displacement on the Zuccale fault are illustrated in the geological cross section across eastern Elba Island (Fig. 1c). Along this section, the main tectonic contact between upper complex and lower complex is displaced eastward by about 6 km, as also reported by Keller and Coward (1996).

3.1. The contact aureole of the Porto Azzurro pluton

In eastern Elba Island, the emplacement of the Porto Azzurro pluton (5.9–6.2 Ma; Musumeci et al., 2011; Maineri et al., 2003) led

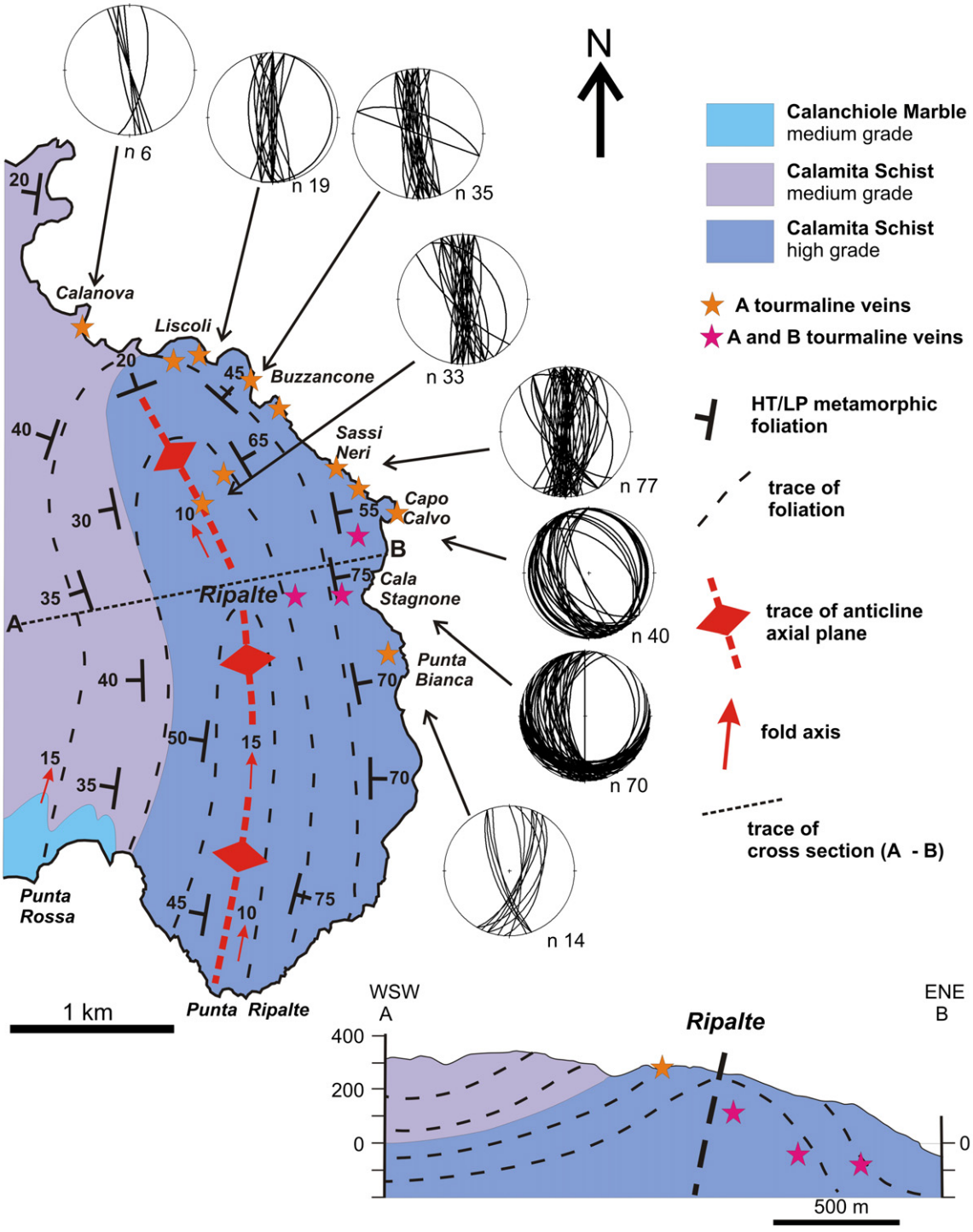

Fig. 3. Geological sketch map of the hinge zone of the Ripalte antiform (eastern Calamita peninsula) showing the areal distribution of tourmaline-rich veins and the location of measured sections (stars). Equal-area lower-hemisphere stereographic projections plot great circle orientations of tourmaline veins measured at selected localities exposed along the east coast of the Calamita Peninsula.

to the development of a wide contact aureole (about 6–7 km in diameter) affecting the Calamita and Ortano units. Contact metamorphism, dated at 6.2 Ma (Ar/Ar muscovite ages; Musumeci et al., 2011), largely overprints an early-middle Miocene foliation in the Calamita Schist (Pertusati et al., 1993). The wide extent of the contact aureole, which underlies the entire Calamita peninsula (Figs. 1 and 2a), indicates that the Porto Azzurro pluton is much larger than the restricted exposure of medium-grained biotite monzogranite north of the Calamita peninsula (Fig. 1b). Moreover, gravimetric data from the northern Calamita peninsula (Siniscalchi et al., 2008) and the intersection of granitic rocks at depths of 150–200 m in boreholes in eastern Elba Island (Bortolotti et al., 2001) strongly suggest that the pluton roof occurs at very shallow depth.

Duranti et al. (1992) documented a sequence of prograde metamorphic zones in the contact aureole, ranging from biotite zone to andalusite-k-feldspar zone in the pelitic/psammitic hornfelses and from biotite zone to wollastonite zone in the carbonate

hornfelses. The estimated P-T conditions ranges from 300 °C (biotite zone) to 650 °C (andalusite-K-feldspar zone and wollastonite zone), with Pmax < 0.18–0.2 GPa (Duranti et al., 1992). These P–T conditions indicate that the Porto Azzurro pluton was emplaced at a very shallow crustal level into the metamorphic units of the lower complex.

The Calamita Schist, hosting the Porto Azzurro pluton, represents the inner portion of the contact aureole and consists of medium- to high-grade hornfels with biotite + muscovite + andalusite + cordierite + K-feldspar mineral assemblages (Mazzarini and Musumeci, 2008). Metamorphic grade increases eastward across the Calamita Peninsula and the highest grade hornfelses crop out in the eastern part where they are intruded by leucogranitic sills and dykes derived from the Porto Azzurro pluton (Fig. 2a).

3.2. Ripalte Antiform, Calamita peninsula

In the Calamita Penisula, the foliation attitudes within the Calamita Schist define a large scale, gently NNW-plunging antiform (Fig. 2a, b, c) cored by high metamorphic grade hornfelses. The hinge zone of this structure crops out in the Ripalte area in the eastern Calamita Peninsula (Figs. 2 and 3). It is a steeply-inclined, asymmetric fold, overturned toward the east, with gently- to moderately-dipping foliation in the western back limb and steeply-dipping foliation in the eastern forelimb. The latter crops out in the easternmost part of the Calamita peninsula, extending from Liscoli in the north to Punta delle Ripalte in the south. The fold axis plunges ~20° north and the periclinal termination of the fold crops out in the Liscoli area, where the foliation dips gently to moderately toward the NW and NE (Figs. 2a and 3). Minor fold structures (antiforms and synforms) as well as reverse faults with top to the east sense of shear occur in the back limb of the Ripalte antiform, affecting the Calamita Unit (Calamita Schist and Calanchiole Marble; Fig. 2a,b).

In the field, deformation associated with the Ripalte antiform is accompanied by NNW–SSE trending mesoscopic open folds of decimeter to meter wavelength with upright to west-dipping axial planes (Fig. 4a). Deformation intensity increases toward the hinge zone of the antiform (Figs. 2 and 3), where close to tight, gently north (10°–20°) plunging minor folds are observed together with a spaced to continuous axial-plane crenulation cleavage (Fig. 4b,c). The latter, marked by biotite and muscovite growth, leads locally to almost complete transposition of the previous foliation and the contact metamorphism mineral assemblages (Fig. 4c).

4. The tourmaline-rich vein system of Eastern Elba Island

4.1. Tourmaline veins

A system of tourmaline-rich veins occurs on the eastern side of Calamita peninsula from north of Calanova to south of Punta Bianca (Figs. 3 and 2c). The veins are filled by fine- to very fine-grained black (schorl-dravite) and/or brownish (uvite) tourmaline. Their composition records the circulation of magmatic, boron-rich hydrothermal fluids that partly interacted with the host rocks (Dini et al., 2008).

The tourmaline veins were emplaced into high-grade hornfels of the Calamita Schist in a structural position corresponding to the hinge and eastern flank of the Ripalte antiform. They are characterized by an uneven spatial distribution from Barbarossa in the north and Punta Bianca in the south, with the highest density occurring in the Cala Stagnone – Capo Calvo area. The tourmaline-rich vein system has been examined in several well-exposed

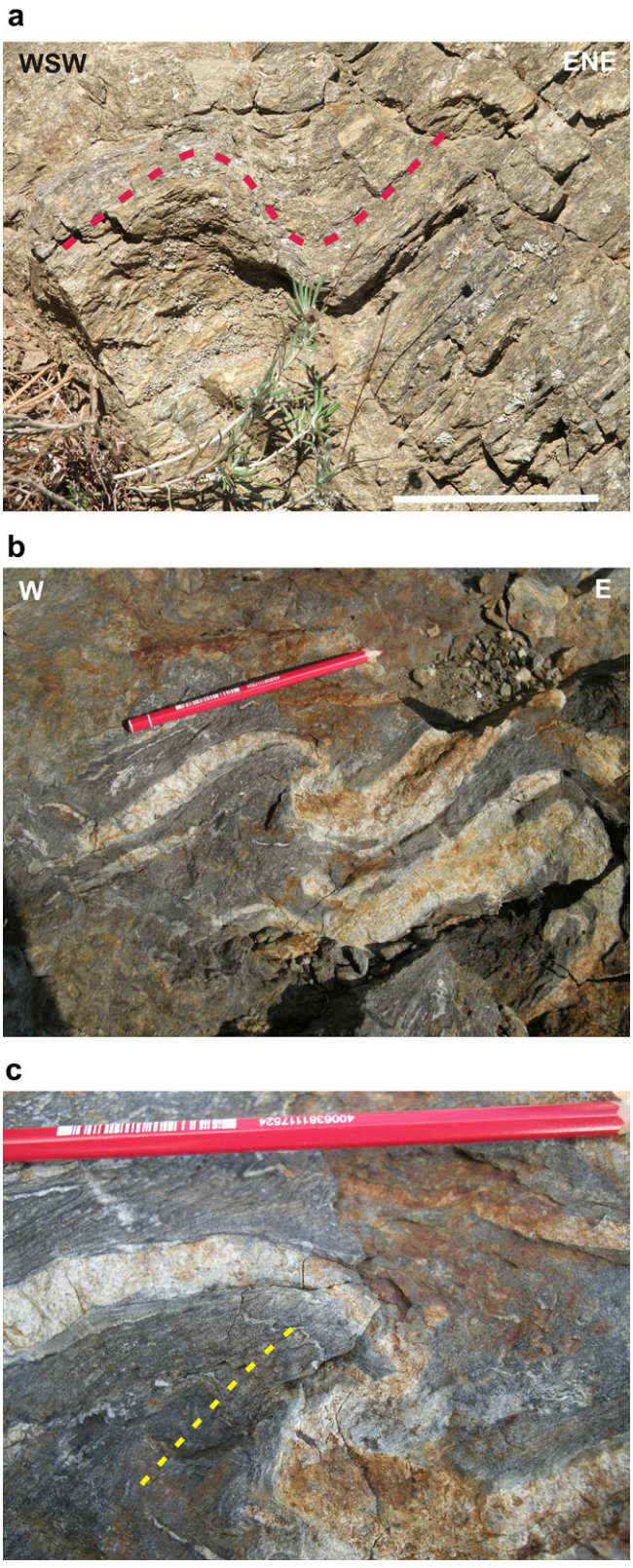

Fig. 4. Photographs of fold structures in the Calamita Schist. a) Open fold in the western limb of the Ripalte antiform; b) tight asymmetric fold overturned toward the east in the high-grade hornfels of the eastern limb of the Ripalte antiform (Punta Bianca); c) detail of Fig. b showing well developed axial-plane crenulation cleavage in pelitic (And + Bt + Kfs) layers with local transposition of previous foliation along fold limbs.

outcrops along a ~3 km long, N–S section (star symbols in Fig. 3). The veins mainly strike N–S to NW–SE and a few strike WNW–ESE (Fig. 2d). Two vein sets (A veins and B veins) have been defined on the basis of their strike and dip distributions as well as infilling material. Observed relative abutting relationships between the two vein sets indicates coeval emplacement.

The A-set (207 veins) comprises steeply-dipping veins that are well clustered around N–S to NNW–SSE strike directions (Fig. 5a). This set is distributed throughout the studied section (Fig. 3) and it is composed only of black tourmaline veins (Fig. 6a). The A-set veins are mode I fractures associated with a dextral component of shear as indicated by steeply-dipping en-echelon vein arrays (Fig. 6b,c).

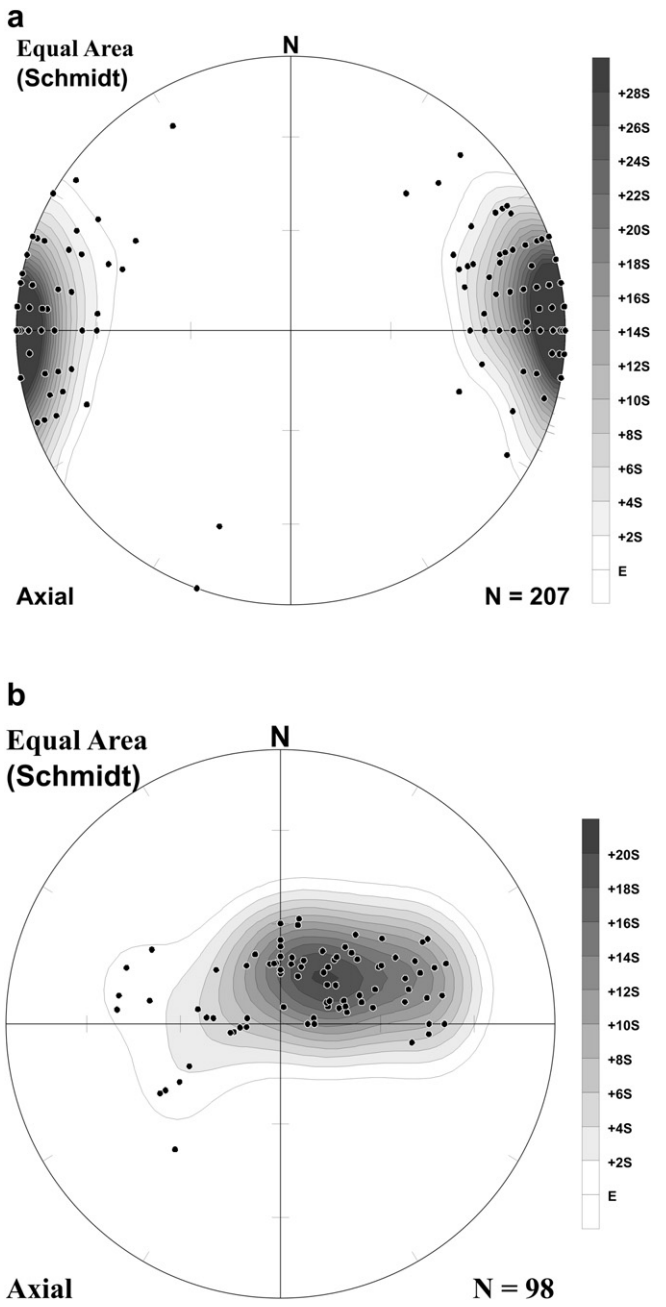

Fig. 5. Equal-area lower-hemisphere projections of poles to veins. a) A-set vein data. b) B-set vein data. Contouring is done by the numbers of counts (E) expressed as multiplies of the standard deviation (S).

The B-set (98 veins) is mostly concentrated in the Cala Stagnone and Capo Calvo area (Fig. 3) and is characterized by gentle to moderate dips and a dispersed strike distribution around a dominant NW–SE trend and a minor E–W trend (Figs. 5b and 6d). These veins are filled by black tourmaline (schorl-dravite) and by brownish tourmalines (uvite) (Dini et al., 2008). The B-set is characterized by extensional shear veins and Mode I aperture veins; locally B-set veins show evidence for hydraulic fracturing associated with breccia formation (Fig. 6e). Several B-set veins formed by exploiting shear zones as indicated by slickensides composed of tourmaline fibres observed in vein walls. Most of the observed shear zones are reverse faults with top to N and NNW sense of movement (Fig. 6f).

4.2. Vein geometry and size distributions

The thickness (W) to length (L) aspect ratio (W/L) has been determined for tourmaline veins that meet the following criteria (see Gudmundsson, 1999): i) mode I veins with no appreciable shear displacement; and ii) veins that do not intersect other fractures, veins or rock discontinuities (unrestricted veins). Using these criteria, 29 samples were measured; 14 in the A set and 15 in the B set. W/L ratios of all veins vary between 0.001 and 0.033 with an average of 0.005; for the A set the range is 0.001–0.005 with an average of 0.003 and for the B set the range is 0.001–0.033 range with an average of 0.006 (Table 1). Field observations are consistent with the measured aspect ratios confirming that A-set veins are longer and thinner than B-set veins.

The thickness of 282 veins was measured in the field; 216 from the A set and 54 from the B set. Because the veins are spread along a ~3 km long coastal section (Fig. 3), we have not measured along a continuous transect; in order to avoid an oversampling of large veins, we measured thickness at several distinct sites, a few hundred of meters apart, paying attention to sampling veins only once at each site. Overall, vein thicknesses range between 0.05 and 25 cm with a mean of 1.8 cm (Table 1). A-set veins have thicknesses varying from 0.1 to 16.5 cm with an average of 1.5 cm, and B-set veins have thicknesses ranging from 0.05 to 25 cm with an average of 2.7 cm (Table 1).

The spacing of veins was measured along transects normal to the very steeply-dipping A-set, resulting in 119 measurements. The A-set vein spacing ranges between 0.5 and 150 cm with an average of 20.3 cm (Table 1). Due to exposure conditions, only a visual estimate could be made for the B-set veins, which have an apparent spacing between 40 and 50 cm up to 1.2 m (Fig. 6d).

The distributions of veins thicknesses (A and B sets) and the spacing of A-set veins are clustered, as their coefficients of variation (C_v) are >1 (Table 2), and they are well described by power-law distributions (Fig. 7). The thicknesses of all the veins have a fractal exponent of ~1.85 in the 1.8–24 cm size range (Table 3). The spacing distribution of the A-set veins has a fractal exponent of ~0.68 in the 3–50 cm size range (Table 3). The thickness distributions suggest that B-set veins are thicker than A veins. Indeed, B-set veins have a thickness distribution with a lower fractal exponent (a ~ 1.35) than the A-set veins (a ~ 2.04), and the size range for the B-set veins is 2.2–24 cm compared to 2.4–16 cm for the A-set veins (Table 3). The theoretical maximum values of distributions for all the analyzed data sets (W_{MAX} in Table 3) are very close to the empirical maximum (i.e., the observed maximum thicknesses measured in the field), indicating that the actual thickness distribution of the veins is well sampled. Conversely, the observed maximum spacing (S_{MAX}) values of the A-set veins is lower than the theoretical value (Table 3), indicating that censoring

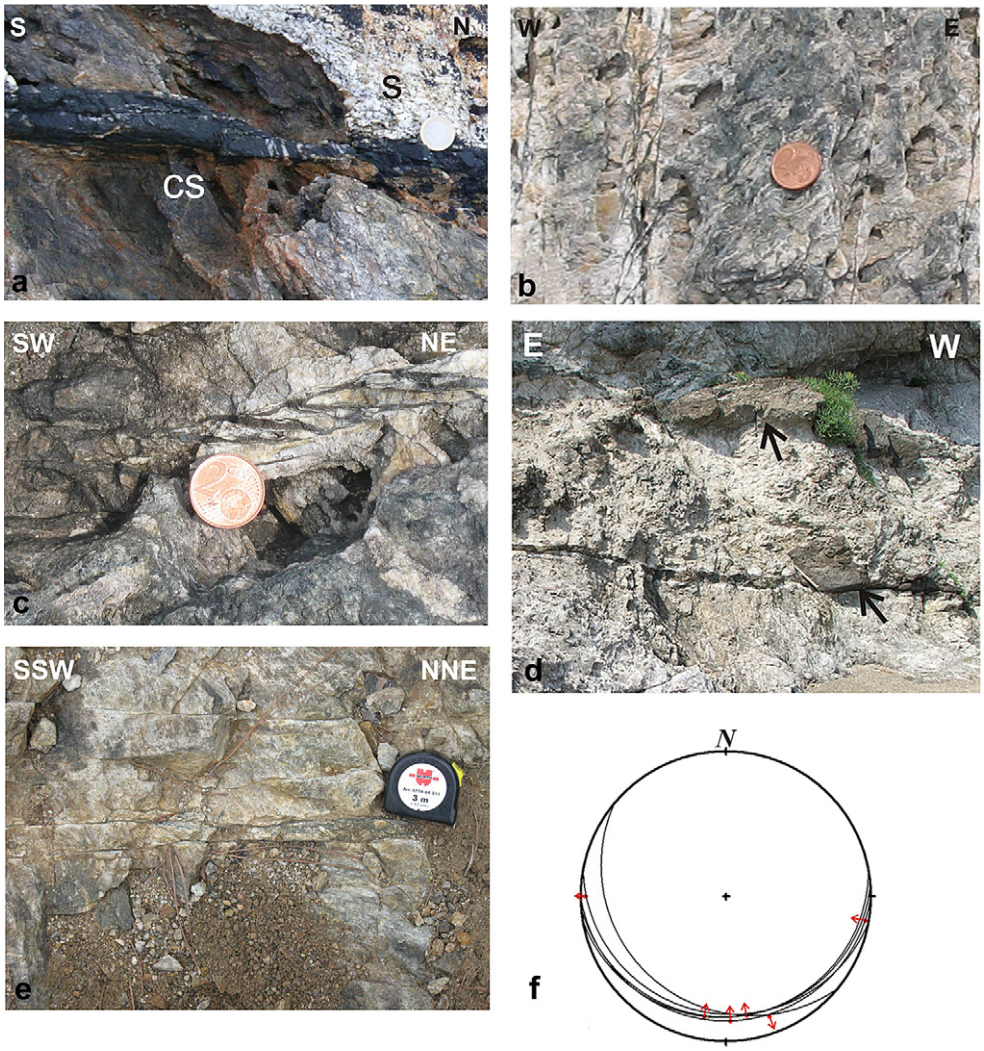

Fig. 6. a) Dilational A-set veins cross cutting Calamita Schist (cs) and leucogranite sills (s); diameter of coin is 2.2 cm. b) Dilatational and extensional shear A-set veins; diameter of coin is 1.9 cm. c) Extensional shear A-set vein with right-lateral motion as indicated by the orientation of en-echelon strands; diameter of coin is 1.9 cm. d) B-set veins cross cutting Calamita Schist; the distance between the two veins (black arrows) is about 1.2 m. e) Hydrofracturing in a B-set vein; measuring tape is ~6 cm long. f) Equal-area lower-hemisphere projection of shear zones and slip directions (red arrows) observed in some of the B-set veins; most of the data indicate a top to N to NW movement.

effects predominate the spacing analysis and that the exponent is overestimated.

4.3. State of stress

The Calamita Peninsula tourmaline veins comprise two distinct data sets with differently clustered pole distributions. The B-set has a clustered distribution around a steeply plunging inferred σ_3 direction whereas the A-set is well clustered around a nearly horizontal inferred σ_3 direction (Table 4 and Figs. 5 and 8). Attribution of eigenvectors to the appropriate principal stress has been done by choosing the θ_2 and θ_1 angles for which $\Phi < 1$. The pole distribution of veins defines $\theta_2 = 61°$ and $\theta_1 = 50°$ for the A-set veins and $\theta_2 = 47°$ and $\theta_1 = 26°$ for the B-set veins (Fig. 8; Table 4). According to Jolly and Sanderson (1997), the θ_2 and θ_1 angles for both vein sets indicate conditions with $P_f < \sigma_2$ (Fig. 8). From Equations (5) and (7), we obtain $\Phi = 0.57$ and $R' = 0.24$ for the A-set veins and $\Phi = 0.58$ and $R' = 0.47$ for the B-set veins. The Mohr circle configuration for the stress field at the time of vein formation has been derived for each data set by using the computed stress and driving pressure ratios (Fig. 8). The diagrams indicate that both sets of veins likely formed under extensional shear conditions (Fig. 8), consistent with field observations.

Table 1
Statistics of aspect ratio, spacing and thickness (W) of tourmaline veins.

Data	Aspect ratio (W/L)					Spacing (cm)					Thickness (W) (cm)				
	n	Max	Min	Mean	σ	*n*	Max	Min	Mean	σ	*n*	Max	Min	Mean	σ
All	29	0.033	0.001	0.005	0.006						282	25	0.05	1.8	2.8
A	14	0.008	0.001	0.003	0.001	119	150	0.5	20.3	32.5	216	16.5	0.1	1.5	2.2
B	15	0.033	0.001	0.006	0.007						54	25	0.05	2.7	4.4

Data: data set; *n*: sample number; σ: standard deviation.

Table 2
Coefficient of variation C_v of spacing and thickness distributions of tourmaline veins.

Data	Spacing	Thickness
All	–	1.6
A	1.4	1.5
B	–	1.6

Data: data set.

4.4. Depth of vein formation and fluid overpressure

The thermal peak of contact metamorphism in the host rocks developed under LP–HT conditions ($P_{max} < 0.20$ GPa, e.g., Mazzarini and Musumeci, 2008), corresponding to a maximum depth of 5–6 km. The tourmaline veins are genetically related to late-intrusive events in eastern Elba Island and were generated as hydrofractures emanating from metasomatic bodies at the contact between igneous intrusions and their country rocks (Dini et al., 2008). Hydrofractures and metamorphic veins develop rapidly (≤200 yr) relative to rates of metamorphic processes, as demonstrated for veins in metamorphosed Cretaceous limestone in the Hiraodai Fukuoka Prefecture, Japan (Nishiyama, 1989). These considerations tightly associate tourmaline veins to the late-magmatic events on Elba Island in time and space. Mazzarini and Musumeci (2008) concluded that the leucogranitic sills of the Calamita Peninsula, associated with the Porto Azzurro pluton, were emplaced at a maximum depth of about 3 km. Therefore the depth of tourmaline vein formation is also assumed to be close to 3 km.

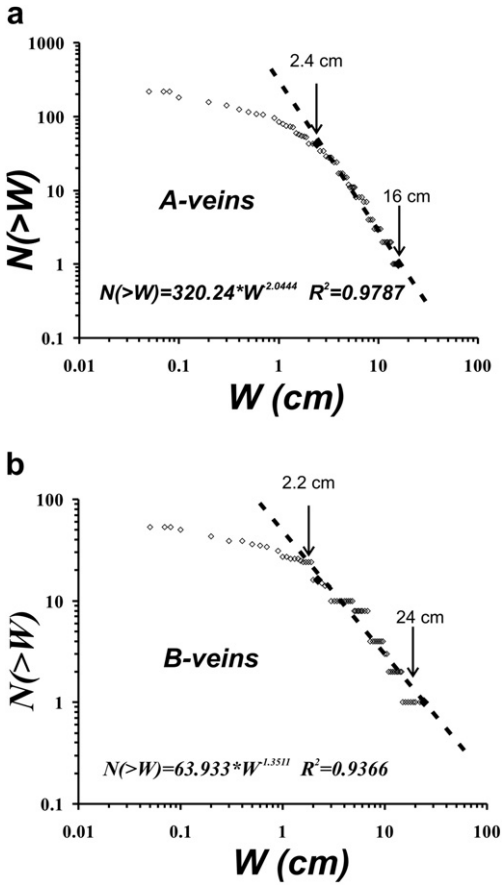

Fig. 7. Logarithmic plot of vein thicknesses. Dashed lines are best fit lines for the distribution of the population. a) N (>W) vs W (cm) for A-set veins. b) N (>W) vs W (cm) for B-set veins.

Table 3
Power-law distributions for thickness and spacing of tourmaline veins.

Data	Thickness (W)					
	n	c	a	R^2	s.r. (cm)	W_{MAX} (cm) – S_{MAX} (m)
All	282	376.23	1.8484	0.9612	1.8–24	24.7
A	216	320.24	2.0444	0.9787	2.4–16	16.8
B	54	63.933	1.3511	0.9366	2.2–24	21.7
	Spacing (S)					
A	119	205.48	0.6794	0.9936	3–50	25.4

Data: data set; n: sample number; c: normalization constant; a: fractal exponent; R^2: goodness of fit; s.r.: size range; W_{MAX}: theoretical maximum thickness of the power-law distribution; S_{MAX}: theoretical maximum spacing of the power-law distribution.

The fluid overpressure ($\Delta P_o = P_f - \sigma_3$) at the time of vein formation can be estimated by applying Equation (8) and using the average values of the tourmaline vein aspect ratio (W/L). The Young's modulus (E), Poisson's ratio (ν) and tensile strength (T_o) of the Calamita Schist are not known directly. We therefore adopt values derived from the elastic parameters of lithologies that best approximate the mechanical behavior of this unit (i.e., quartzite, shale, sandstone and schist). The following ranges of elastic parameters were derived from the literature: $E = 5–20$ GPa, $\nu = 0.11–0.40$ and $T_o = 5–10$ MPa (Lama and Vutukuri, 1978; Jaeger and Cook, 1979; Turcotte and Schubert, 2002; Nasseri et al., 2003; Gerecek, 2007).

Given the uncertainty in host-rock elastic properties, the estimated fluid overpressure varies in the range 3–95 MPa for the A-set veins and 3–119 MPa for the B-set veins. Following Mazzarini and Musumeci (2008), we assume a Poisson's ratio of 0.25 and a Young's modulus of 10 GPa as likely values for the Calamita Schist. The resulting average fluid overpressures are ~16 MPa for the A-set veins and ~32 MPa for the B-set veins, respectively. Taking into account that $\Delta P_o = P_f - \sigma_3$ and assuming that $\sigma_3 = T_0 = 5$ MPa (see Mazzarini and Musumeci, 2008) the P_f derived from the structural data is 21 MPa for the A-set veins and 37 MPa for the B-set veins. Assuming a formation depth of about 3 km, the A-set veins formed under sub-hydrostatic ($\lambda < 0.4$) conditions, whereas the B-set veins formed under supra-hydrostatic conditions ($\lambda > 0.4$).

5. Discussion

The tourmaline veins of eastern Elba Island are spatially and genetically related to the Porto Azzurro intrusion (Dini et al., 2008). Our data show that the veins are not evenly distributed in the thermal aureole and consist of two well-defined sets (A and B-set veins). Field observations suggest that the B-set veins have a lower spacing than the A-set veins. The thickness distribution of the B-set veins is characterized by a fractal exponent that is lower than that of the A-set veins (Table 3). According to Monecke et al. (2001), the fractal thickness distribution of the B-set veins implies that they formed under high growth-rate conditions, resulting in thick veins. This is consistent with the observation that the B-set veins are thicker than the A-set veins (Table 1). Moreover, the estimated fluid overpressure for the B-set veins is higher than that of the A-set veins. The pole distribution of the B-set veins is consistent with

Table 4
Stress and driving pressure ratios of tourmaline veins.

Data set	θ_2	θ_1	σ_1	σ_2	σ_3	Φ	R'
A	61°	50°	181°/46°	354°/44°	87°/3°	0.57	0.24
B	47°	26°	170°/10°	263°/15°	47°/72°	0.58	0.47

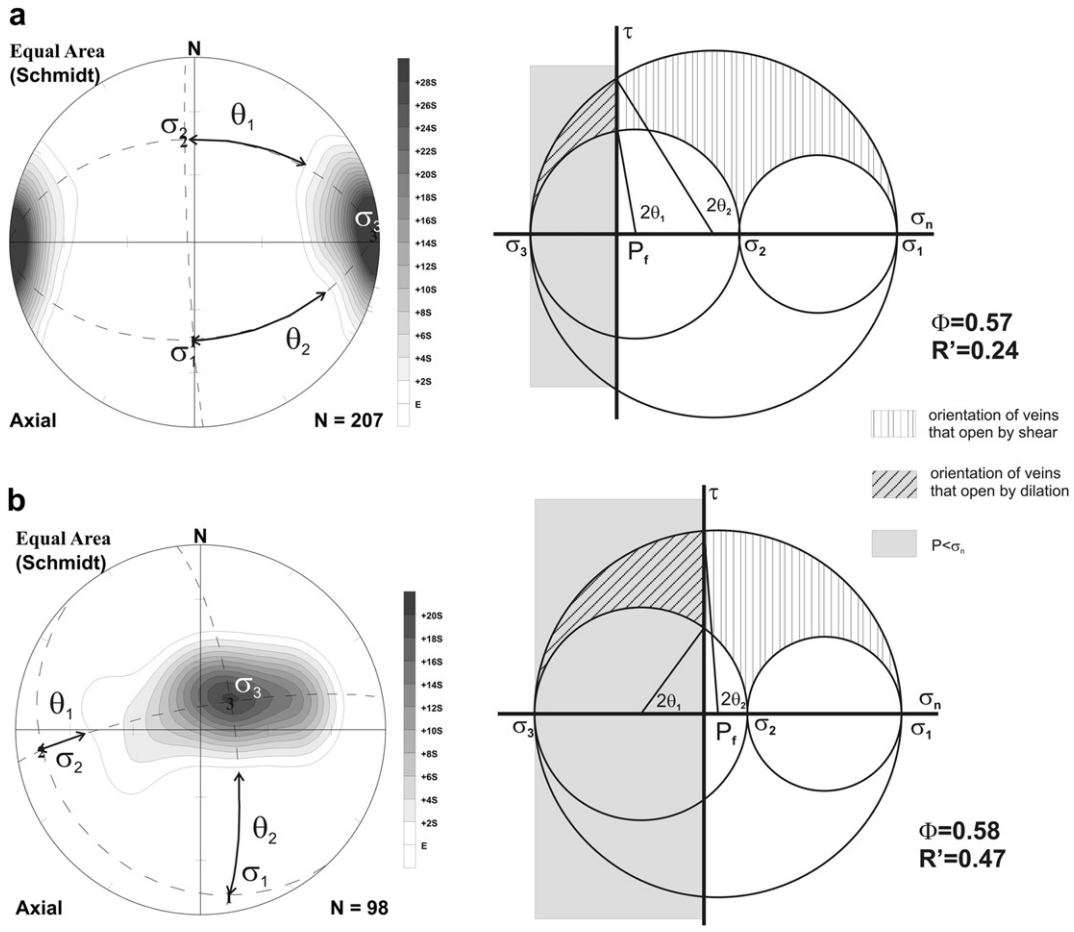

Fig. 8. a) Contoured equal-area lower-hemisphere projections of poles to A-set veins showing the derivation of the principal stress directions and the θ_1 and θ_2 angles (left) and the resulting Mohr circle diagram (right) using $\Phi = 0.57$, $R' = 0.24$, $2\theta_2 = 122°$, and $2\theta_1 = 100°$. b) Contoured equal-area lower-hemisphere projections of poles to B-set veins and the resulting Mohr circle diagram using $\Phi = 0.58$, $R' = 0.47$, $2\theta_2 = 94°$, and $2\theta_1 = 52°$. Shaded areas represent zones where $\sigma_n < P_f$, hatched areas represent the orientation of veins that undergo dilation or dilation and shearing.

a local stress field with nearly vertical σ_3 and nearly horizontal σ_1 and σ_2 (Fig. 8). On the other hand, the pole distribution of the A-set veins is consistent with a local stress field with nearly horizontal σ_3 and moderately plunging σ_2 (44°) and σ_1 (46°).

In the hinge zone of the Ripalte anticline, the B-set veins are characterized by horizontal σ_1 sub-parallel to the fold axis, while the A-set veins indicate a moderately northwest-plunging σ_2 with the σ_1–σ_2 plane close to the axial surface orientation of the antiform (Fig. 8). A-set tourmaline veins generally strike parallel or sub-parallel to the direction of the fold axis.

The different stress orientations deduced for the two vein sets (Table 4 and Fig. 8) are consistent with the development of vein systems above and below the neutral surface of a parallel, flexural-flow fold (e.g., Price and Cosgrove, 1990). The A-set veins, with horizontal σ_3, formed above the neutral surface in response to outer-arc stretching (Fig. 9). Conversely, the B-set veins formed below the neutral surface in response to inner-arc shortening. This accounts for the estimated high fluid pressure and the observation of associated extensional shear during vein emplacement (B-set veins; Fig. 6f). Moreover, the occurrence of shear during fracture formation associated with folding is consistent with the $P_f < \sigma_2$ conditions derived for the veins (see Mohr diagrams in Fig. 8). Indeed, Price and Cosgrove (1990) suggest that σ_1 parallel to a fold axis may indicate fluid pressure less than the intermediate stress (σ_2) and sufficiently large σ_1 to induce shear failure (i.e., $(\sigma_1 - \sigma_3) > 4T_0$; Sibson, 2000). The local stress field in which fractures formed may not be homogeneous from limb to hinge, or symmetrically oriented with respect to the far-field principal stress axes, as suggested by field relationships between folding and fracturing in the Emigrant Gap anticline, Wyoming, USA (Bergbauer and Pollard, 2004).

Propagation of veins during fault-bend folding has been reported by Srivastava and Engelder (1990) in the Appalachian Valley and Ridge (Pennsylvania, USA). Extension is favored above the neutral surface in the hinge zone of a fault-bend anticline, whereas contraction dominates below the neutral surface (Srivastava and Engelder, 1990). In naturally deformed rocks, multiple fracture sets form symmetrically with respect to the fold axis and differentiate spatially with respect to the neutral surface (Stearns, 1968). For example, in the detachment folds in the Monterrey Salient (Mexico) sub-vertical late-stage veins (strike veins) formed parallel to the fold axis in the hinge zone. These veins, which accommodated fold axis perpendicular extension of the anticline crest, formed during fold tightening, outer-arc stretching and concomitant upward migration of fluids from the fold core (Fischer et al., 2009).

According to Ramsay and Huber (1987), the finite neutral surface should migrate toward the inner arc during fold growth in order to maintain strain compatibility. This implies that at every stage of folding an incremental neutral surface (INS) is located on the inside of the finite neutral surface (FNS), separating zones of active layer stretching and active layer shortening.

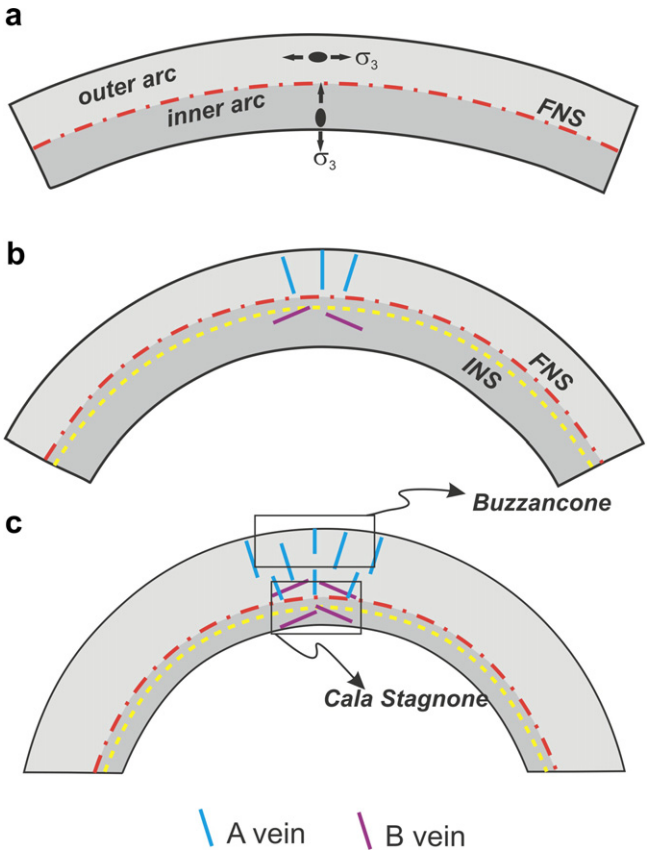

Fig. 9. Conceptual model of the tectonic environment for the formation of tourmaline veins in the Calamita Peninsula. FNS = finite neutral surface (dot-dashed red line); INS = incremental neutral surface (dashed yellow line). a) Buckle folding with extension (horizontal σ_3) in the outer arc and compression (vertical σ_3) in the inner arc; ellipses represent the finite strain. b) First stage: in the outer arc of the hinge zone, extension allows the formation of extensional veins (A set; blue) whereas inner-arc compression favors the formation of nearly horizontal shear zones and veins (B set; purple). c) Final stage: as the fold thickens and amplifies the incremental neutral surface moves toward the core of the fold, previous shear veins are now above the INS and are overprinted by steeply-dipping extensional veins.

With the above points in mind, we propose the following model for the formation of tourmaline veins in the Calamita peninsula (Fig. 9a). At earlier stages, B-set veins formed as extensional shear veins exploiting inner arc shear zones (i.e., below the FNS) where layer shortening is dominant, while in the outer arc, A-set veins formed as extensional fractures (Fig. 9b). As deformation proceeded, the INS moved toward the core of the antiform, below the early-formed B-set veins, giving rise to the formation of new A-set and B-set veins (Fig. 9c).

Therefore, the local switch of the minimum stress axis due to fluid overpressure invoked by Dini et al. (2008) to explain the two different vein orientations in the Cala Stagnone area can instead be readily explained as consequence of incremental neutral surface migration due to fold amplification (see Ramsay and Huber, 1987). The second episode of fracture opening and fluid injection into the B-set veins described in Dini et al. (2008) at Cala Stagnone can also be explained as consequence of the passage of this rock volume above the INS and the interaction of early B-set veins with outer-arc extension.

The proposed large scale folding model is also in agreement with recent detailed structural analysis of leucogranite sill distributions in the Calamita Peninsula and their geometric relationships with host-rock foliations (Cruden et al., 2009). These new data show that the sills are consistently oriented at shallow oblique angles to the wall-rock foliation. The obliquity between sills and foliation is interpreted to indicate syn-tectonic emplacement in the fore- and back-limbs of the Ripalte antiform (Cruden et al., 2009). The kilometer-scale wavelength, the upright attitude, the asymmetric shape and the constant eastward vergence from the back limb to the forelimb of the Ripalte antiform are features that are consistent with horizontal shortening related to regional deformation, instead of local vertical shortening prior to or during to pluton inflation (c.f., Smith et al., 2011). Furthermore, at regional scale, recent investigations highlight that the emplacement of Pliocene granites in the coastal area of southern Tuscany occurred during crustal shortening (Boccaletti and Sani, 1998; Musumeci et al., 2005, 2008; Sani et al., 2009).

In the Calamita Peninsula, the development of a high-temperature hydrothermal system during late Miocene shortening of the contact aureole of the Porto Azzurro pluton raises questions about the role and timing of regional extensional at this time (e.g., Collettini et al., 2006). Field evidence from the north-eastern part of the Calamita peninsula, west of Porto Azzurro, indicates that the Zuccale Fault crosscuts the contact aureole and NS trending minor folds related to the Ripalte antiform (Figs. 1 and 2). Furthermore, the eastward displacement of contact metamorphic-related isograds in the hanging wall of the Zuccale Fault (Duranti et al., 1992), the dominant occurrence of cataclasites within the fault containing abundant clasts of pelitic and carbonate hornfelses, and the absence of igneous intrusions cross cutting the fault zone (Mazzarini and Musumeci, 2008) all constitute evidence that the Zuccale Fault largely postdates granite emplacement and contact metamorphism (Pertusati et al., 1993). Together, these observations argue against the coeval development of extensional faulting and granite emplacement in eastern Elba Island, and more broadly within the northern Tyrrhenian Sea region (e.g., Rossetti et al., 1999; Acocella and Rossetti, 2002). The collective evidence leads us to propose that the Ripalte Antiform and coeval tourmaline vein emplacement within the contact aureole of the Porto Azzurro pluton formed as result of horizontal shortening. This was followed by extension, assuming that the Zuccale Fault is a low-angle normal fault (e.g., Collettini et al., 2006).

Recently, Smith et al. (2011) have proposed that the outcrop distribution of the Zuccale Fault in the Calamita peninsula defines a domal structure, which they ascribe to vertical inflation (laccolith growth) of the Porto Azzurro pluton during regional extension. However, as seen in geological section (Fig. 1c) and from the observations discussed above, the proposed WNW–ESE trending dome (see Fig. 3 in Smith et al., 2011) should have developed after contact metamorphism, hydrothermal circulation and large scale folding.

Since the Porto Azzurro contact aureole may represent a proxy for HT geothermal systems, the proposed tectonically-driven mechanism for tourmaline vein development provides new insight on high-temperature deep-seated reservoirs in the Larderello-Travale geothermal field (e.g., Bertini et al., 2006), where highly fractured zones associated with circulation of high-temperature fluids (e.g., H and K horizons, Casini et al., 2010) are located in a contact aureole.

6. Conclusions

A high-temperature hydrothermal system in the contact aureole of the Porto Azzurro pluton (eastern Elba Island) is recorded by the formation of tourmaline veins that are spatially and genetically related to tabular leucogranitic intrusions. Structural analysis of the veins and their host rock indicates that fluid circulation was confined to the core of a growing anticline, within the inner portion of the thermal aureole. Secondary permeability in the deforming

thermal aureole was controlled by ongoing deformation associated with the development of fracture systems in the hinge zone of the fold that favored transport and localization of fluids. This example of localization of fluid flow within a tectonically active structure has important implications for the exploitation of high-temperature reservoirs in geothermal fields.

The kilometer-scale folding of the Porto Azzurro pluton's contact aureole is consistent with a regime of regional horizontal shortening, rather than deformation due to syn-extensional granite emplacement. Further geological and geophysical investigations are required to better define the role and significance of this structure in the context of the late Neogene tectonics of the northern Tyrrhenian Sea.

Acknowledgments

ARC thanks the INGV for funding a sabbatical visit to the Pisa section and funding from a Natural Sciences and Engineering Research Council of Canada Discovery Grant. We thank F. Camposano for assistance during fieldwork. We thank K.W.H. McCaffrey and an anonymous reviewer for comments that improved the manuscript.

References

Acocella, V., Rossetti, F., 2002. The role of extensional tectonics at different crustal levels on granite ascent and emplacement: an example from Tuscany (Italy). Tectonophysics 354, 71–83.

André, A.-S., Sasse, J., Lespinasse, M., 2001. New approach for the quantification of paleostress magnitudes: application to the Soultz vein system (Rhine graben, France). Tectonophysics 336, 215–231.

Angelier, J., 1984. Tectonic analysis of fault slip data sets. Journal of Geophysical Research 89, 5835–5848.

Baer, G., Beyth, M., Reches, Z., 1994. Dikes emplaced into fractured basement, timma igneous complex, Israel. Journal of Geophysical Research 99, 24039–24050.

Barberi, F., Giglia, G., Innocenti, F., Marinelli, G., Raggi, G., Ricci, C.A., Squarci, P., Taffi, L., Trevisan, L., 1967. Carta geologica dell'isola d'Elba scala 1:25.000. C.N.R., Roma.

Bartole, R., 1995. The north Tyrrhenian-northern Apennines post-collisional system: constraints for a geodynamic model. Terra Nova 7, 7–30.

Bergbauer, S., Pollard, D.D., 2004. A new conceptual fold-fracture model including prefolding joints, based on the Emigrant Gap anticline, Wyoming. Geological Society of America Bulletin 116, 294–307. doi:10.1130/B25225.1.

Bertini, G., Casini, M., Gianelli, G., Pandeli, E., 2006. Geological structure of a long-living geothermal system, Larderello, Italy. Terra Nova 18, 163–169.

Boccaletti, M., Elter, P., Guazzone, G., 1971. Plate tectonics models for the development of Western Alps and Northern Apennines. Nature 234, 108–111.

Boccaletti, M., Sani, F., 1998. Cover thrust reactivations during Neogene-Quaternary evolution of the northern Apennines. Tectonics 17, 112–130.

Bonnet, E., Bour, O., Odling, N., Main, I., Berkowitz, B., Davy, P., Cowie, P., 2001. Scaling of fracture systems in geological media. Reviews of Geophysics 39, 347–383.

Bortolotti, V., Fazzuoli, M., Pandeli, E., Principi, G., Babbini, A., Corti, S., 2001. Geology of central and eastern Elba Island, Italy. Ofioliti 26, 97–105.

Bossio, A., Costantini, A., Foresi, L.M., Lazzarotto, A., Mazzanti, R., Mazzei, R., Pascucci, V., Salvatorini, G., Sandrelli, F., Terzuoli, A., 1998. Neogene-Quaternary sedimentary evolution in the western side of the northern Appennines (Italy). Memorie della Società Geologica Italiana 52, 513–525.

Bouillin, J.P., 1983. Exemples de deformation locale liées à la mis en place de granitoides alpins dans des conditions distensives: l'ile d'Elbe (Italie) et le Cap Bougaron (Algérie). Revue de Géologie Dynamique et de Géographie Physique 24, 101–116.

Brace, W.F., 1978. A note on permeability changes in geologic materials due to stress. Pure and Applied Geophysics 116, 627–633.

Byerlee, J.D., 1978. Friction of rocks. Pure and Applied Geophysics 116, 615–626.

Carella, M., Fulignati, P., Musumeci, G., Sbrana, A., 2000. Metamorphic consequences of Neogene thermal anomaly in the northern Apennines (Radicondoli-Travale area, Larderello geothermal field – Italy). Geodinamica Acta 13, 345–366.

Casini, M., Ciuffi, S., Fiordelisi, A., Mazzotti, A., Stucchi, E., 2010. Results of a 3D seismic survey at the Travale (Italy) test site. Geothermics 39, 4–12. doi:10.1016/j.geothermics.2009.11.003.

Clark, M.B., Brantley, S.L., Fisher, D.M., 1995. Power-law vein-thickness distribution and positive feedback in vein growth. Geology 23, 975–978.

Clauset, A., Shalizi, C.R., Newman, M.E.J., 2009. Power-law distributions in empirical data. SIAM Review 51, 661–703. doi:10.1137/070710111.

Collettini, C., De Paola, N., Holdsworth, R.E., Barchi, M.R., 2006. The development and behaviour of low-angle normal faults during Cenozoic asymmetric extension in the Northern Apennines, Italy. Journal of Structural Geology 28, 333–352. doi:10.1016/j.jsg.2005.10.003.

Cruden, A.R., Mazzarini, F., Bunger, A.P., Musumeci, G., 2009. Geometry, scaling relationships and emplacement dynamics of a ca. 6 Ma shallow felsic sill complex, Calamita Peninsula, Elba Island, Italy. Eos Transactions AGU 90 (52) Fall Meet. Suppl., Abstract T13A-1843.

Deino, A., Keller, J.V.A., Minelli, G., Pialli, G., 1992. Datazioni $^{40}Ar/^{39}Ar$ del metamorfismo dell'Unità di Ortano-Rio Marina (Isola d'Elba): risultati preliminari. Studi Geologici Camerti 2, 187–192.

Dini, A., Innocenti, F., Rocchi, S., Tonarini, S., Westerman, D.S., 2002. The magmatic evolution of the late Miocene laccolith–pluton–dyke granitic complex of Elba Island, Italy. Geological Magazine 139, 257–279.

Dini, A., Gianelli, G., Puxeddu, M., Ruggieri, G., 2005. Origin and evolution of Pliocene–Pleistocene granites from the Larderello geothermal field (Tuscan Magmatic Province, Italy). Lithos 81, 1–31.

Dini, A., Mazzarini, F., Musumeci, G., Rocchi, S., 2008. Multiple hydro-fracturing by boron-rich fluids in the late Miocene contact aureole of eastern Elba Island (Tuscany, Italy). Terra Nova 20, 318–326.

Duranti, S., Palmeri, R., Pertusati, P.C., Ricci, C.A., 1992. Geological evolution and metamorphic petrology of the basal sequence of eastern Elba (complex II). Acta Vulcanologica 2, 213–229.

Etheridge, M.A., Wall, V.J., Vernon, R.H., 1983. The role of fluid phase during regional metamorphism and deformation. Journal of Metamorphic Geology 1, 205–226.

Fischer, M.P., Higuera-Diaz, I.C., Evans, M.A., Perry, E.C., Lefticariu, L., 2009. Fracture-controlled paleohydrology in a map-scale detachment fold: insights from the analysis of fluid inclusions in calcite and quartz veins. Journal of Structural Geology 31, 1490–1510.

Franceschini, F., 1994. 'Larderello plutono-metamorphic core complex': metamorfismo regionale ercinico di bassa pressione o metamorfismo di contatto Plio-Quaternario? Studi Geologici Camerti 1, 113–128.

Franceschini, F., 1998. Evidence of an extensive Pliocene–Quaternary contact metamorphism in southern Tuscany. Memorie della Società Geologica Italiana 52, 479–492.

Garfagnoli, F., Menna, F., Pandeli, E., Principi, G., 2005. The Porto Azzurro Unit (Mt. Calamita promomtory, south-eastern Elba Island, Tuscany): stratigraphic, tectonic and metamorphic evolution. Bollettino della Società Geologica Italiana 3, 119–138.

Gerecek, H., 2007. Poisson's ratio values for rocks. International Journal of Rock Mechanics & Mining Sciences 44, 1–13.

Gillespie, P.A., Johnston, J.D., Loriga, M.A., McCaffrey, K.J.W., Walsh, J.J., Watterson, J., 1999. Influence of layering on vein systematics in line samples. In: McCaffrey, K.J.W., Lonergan, L., Wilkinson, J.J. (Eds.), Fractures, Fluid Flow and Mineralization. Geological Society, London, Special Publication, 155, pp. 35–56.

Gianelli, G., Manzella, A., Puxeddu, M., 1997a. Crustal models of the geothermal areas of southern Tuscany (Italy). Tectonophysics 281, 221–239.

Gianelli, G., Ruggieri, G., Mussi, M., 1997b. Isotopic and fluid inclusion study of hydrothermal and methamorphic carbonates in the Larderello Geothermal Field and surrounding areas, Italy. Geothermics 26, 393–417.

Gudmundsson, A., 1999. Fluid pressure and stress drop in fault zones. Geophysical Research Letters 26, 115–118.

Harris, N., McMillan, A., Holness, M., Uken, R., Watkeys, M., Rogers, N., Fallick, A., 2003. Melt generation and fluid flow in the thermal aureole of the Bushveld Complex. Journal of Petrology 44, 1031–1054.

Hedenquist, J.W., Lowenstern, J.B., 1994. The role of magmas in the formation of hydrothermal ore deposits. Nature 370, 519–527.

Jaeger, J.C., Cook, N.G.W., 1979. Fundamentals of Rock Mechanics, third ed. Methuen & Co Ltd, London, 513 pp.

Jolivet, L., Faccenna, C., Goffé, B., et al., 1998. Mid crustal shear zones in post orogenic extension: the northern Tyrrhenian Sea case. Journal of Geophysical Research 103, 12123–12160.

Jolly, R.J.H., Sanderson, D.J., 1997. A Mohr circle construction for the opening of a pre-existing fracture. Journal of Structural Geology 19, 887–892.

Johnston, J.D., McCaffrey, K.J.W., 1996. Fractal geometries of vein systems and the variation of scaling relationships with mechanism. Journal of Structural Geology 18, 349–358.

Keller, J.V.A., Coward, M.P., 1996. The structure and evolution of the Northern Tyrrhenian Sea. Geological Magazine 103, 1–16.

Lama, R.D., Vutukuri, V.S., 1978. Handbook on Mechanical Properties of Rock, vol. II. Trans-tech, Clausthal.

Maineri, C., Benvenuti, M., Costagliola, P., Dini, A., Lattanzi, P., Ruggieri, C., Villa, I.M., 2003. Sericitic alteration at the La Crocetta mine (Elba Island, Italy): interplay between magmatism, tectonics, and hydrothermal activity. Mineralium Deposita 38, 67–86.

Malinverno, A., Ryan, W.B.F., 1986. Extension on the Tyrrhenian sea and shortening in the Apennines as result of arc migration driven by sinking of the lithosphere. Tectonics 5, 227–245.

Mazzarini, F., Isola, I., 2007. Hydraulic connection and fluid overpressure in upper crustal rocks: evidence from geometry and spatial distribution of veins at Botrona quarry, southern Tuscany, Italy. Journal of Structural Geology 29, 1386–1399.

Mazzarini, F., Musumeci, G., 2008. Hydrofracturing related sill and dyke emplacement at shallow crustal level: the eastern Elba Dyke Complex, Italy. In: Thomson, K., Petford, N. (Eds.), Structure and Emplacement of High-Level Magmatic Systems. Geological Society, London, Special Publications, 302, pp. 121–129.

Mazzarini, F., Isola, I., Ruggieri, G., Boschi, C., 2010. Fluid circulation in the upper brittle crust: thickness distribution, hydraulic transmissivity fluid inclusion and isotopic data of veins hosted in the Oligocene sandstones of the Macigno Formation in southern Tuscany, Italy. Tectonophysics 493, 118–138. doi:10.1016/j.tecto. 2010. 07.012.

McCaffrey, K.J.W., Johnston, J.D., 1996. Fractal analysis of a mineralised vein deposit: curraghinalt gold deposit: county tyrone. Mineralium Deposita 31, 52–58.

McCaig, A.M., 1988. Deep fluid circulation in fault zone. Geology 16, 867–870.

McKeagney, C.J., Boulter, C.A., Jolly, R.J.H., Foster, R.P., 2004. 3-D Mohr circle analysis of vein opening, Indarama lode-gold deposit, Zimbabwe: implications for exploration. Journal of Structural Geology 26, 1275–1291.

Monecke, T., Gemmell, J.B., Monecke, J., 2001. Fractal distribution of veins in drill core from the Hellyer VHMS deposit, Australia: constraints on the origin and evolution of the mineralising system. Mineralium Deposita 36, 173–188.

Musumeci, G., Bocini, L., Corsi, R., 2002. Alpine tectonothermal evolution of the Tuscan Metamorphic Complex in the Larderello geothermal field (northern Apennines, Italy). Journal of the Geological Society, London 159, 443–456.

Musumeci, G., Mazzarini, F., Corti, G., Barsella, M., Montanari, D., 2005. Magma emplacement in a ramp thrust anticline: the Gavorrano Granite (northern Apennines, Italy). Tectonics 24, TC6009,. doi:10.1029/2005TC001801.

Musumeci, G., Mazzarini, F., Barsella, M., 2008. Pliocene crustal shortening on the Tyrrhenian side of the northern Apennines: evidence from the Gavorrano antiform (southern Tuscany, Italy). Journal Geological Society of London 165, 105–114.

Musumeci, G., Mazzarini, F., Tiepolo, M., Di Vincenzo, G., 2011. U–Pb and $^{40}Ar–^{39}Ar$ geochronology of Palaeozoic units in the northern Apennines: determining protolith age and alpine evolution using the Calamita Schist and Ortano Porphyroid. Geological Journal 46, 288–310. doi:10.1002/gj.1266.

Nabelek, P.I., Labotka, T.C., O_Neil, J.R., Papike, J.J., 1984. Contrasting fluid/rock interaction between the Notch Peak granitic intrusion and argillites and limestones in western Utah: evidence from stable isotopes and phase assemblages. Contribution Mineralogy and Petrology 86, 25–34.

Nasseri, M.H.B., Rao, K.S., Ramamhurty, T., 2003. Anisotropic strength and deformational behavior of Himalayan schists. International Journal of Rock Mechanics & Mining Sciences 40, 3–23.

Norton, D., Knight, J., 1977. Transport phenomena in hydrothermal systems: cooling plutons. American Journal of Science 277, 937–981.

Nishiyama, T., 1989. Kinetics of hydrofracturing and metamorphic veining. Geology 17, 1068–1071. doi:10.1130/ 0091-7613(1989)017<1068:KOHAMV>2.3.CO;2.

Orife, T., Lisle, R.J., 2003. Numerical processing of palaeostress results. Journal of Structural Geology 25, 949–957.

Oliver, N.H.S., 1996. Review and classification of structural controls on fluid flow during regional metamorphism. Journal of Metamorphic Geology 14, 477–492.

Oliver, N.H.S., Valenta, R.H., Wall, V.J., 1990. The effect of heterogeneous stress and strain on metamorphic fluid flow, Mary Kathleen, Australia, and a model for large scale circulation. Journal of Metamorphic Geology 8, 311–331.

Pertusati, P.C., Raggi, G., Ricci, C.A., Duranti, S., Palmeri, R., 1993. Evolusione post-collisionale dell'Elba centro-orientale. Memorie della Società Geologica Italiana 49, 297–312.

Press, W.H., Flammery, B.P., Teukolsky, S.A., Vetterling, W.T., 1986. Numerical Recipes: The Art of Scientific Computing. Cambridge University Press, Cambridge, UK, pp. 818.

Price, N.J., Cosgrove, J.V., 1990. Analysis of Geological Structures. Cambridge University Press, Cambridge. UK, pp. 502.

Ramsay, J.G., Huber, M.I., 1987. Techniques of Modern Structural Geology, 2. Fold and Fractures. Academic Press, London.

Roberts, S., Sanderson, D.J., Gumiel, P., 1999. Fractal analysis and percolation properties of veins. In: McCaffrey, K.J.W., Lonergan, L., Wilkinson, J.J. (Eds.), Fractures, Fluid Flow and Mineralization. Geological Society, London, Special Publication, vol. 155, pp. 71–76.

Rosenbaum, G., Lister, G.S., 2004. Neogene and Quaternary rollback evolution of the Tyrrhenian Sea, the Apennines and the Sicilian Maghrebides. Tectonics 23, TC1013,. doi:10.1029/2003TC001518.

Rosenbaum, G., Gasparon, M., Lucente, F.P., Peccerillo, A., Miller, M.S., 2008. Kinematics of slab tear during subduction and implications for Italian Magmatism. Tectonics 27, TC2008,. doi:10.1029/2007TC002143.

Rossetti, F., Faccenna, C., Jolivet, L., Funiciello, R., Tecce, F., Brunet, C., 1999. Syn-versus post-orogenic extension: the case study of Giglio Island (Northern Tyrrhenian Sea, Italy). Tectonophysics 304, 71–93. doi:10.1016/S0040-1951(98)00304-7.

Ruggieri, G., Gianelli, G., 1999. Multi-stage fluid circulation in a hydraulic fracture breccia of the Larderello geothermal field_Italy. Journal of Volcanology and Geothermal Research 90, 241–261.

Ruggieri, G., Cathelineau, M., Boiron, M.C., Marignac, C., 1999. Boiling and fluid mixing in the chlorite zone of the Larderello geothermal field. Chemical Geology 154, 237–256.

Ruggieri, G., Giolito, C., Gianelli, G., Manzella, A., Boiron, M.-C., 2004. Application of fluid inclusions to the study of Bagnore geothermal field (Tuscany, Italy). Geothermics 33, 675–692.

Sani, F., Bonini, M., Cerrina Feroni, A., Mazzarini, F., Moratti, G., Musumeci, G., Corti, G., Iatta, F., Ellero, A., 2009. Messinian-Early Pliocene crustal shortening along the Tyrrhenian margin of Tuscany, Italy. Italian Journal of Geoscience (Bolletino Società Geologica Italiana) 128, 593–604. doi:10.3301/IJG.2009 128.2.593.

Secor, D.T., 1965. Role of fluid pressure in jointing. American Journal of Sciences 263, 633–646.

Serri, G., Innocenti, F., Manetti, P., 1993. Geochemical and petrological evidence of the subduction of delaminated Adriatic continental lithosphere in the genesis of the Neogene–Quaternary magmatism of central Italy. Tectonophysics 223, 117–147.

Shearer, C.K., Papike, J.J., Simon, S.B., Laul, J.C., Christian, R.P., 1984. Pegmatite/wallrock interactions, Black Hills, South Dakota: progressive boron metasomatism adjacent to the Tip Top pegmatite. Geochimica et Cosmochimica Acta 48, 2563–2579.

Sibson, R.H., 2000. Fluid involvement in normal faulting. Journal of Geodynamics 29, 469–499.

Siniscalchi, A., Diaferia, I., Liuni, M.P., Loddo, M., Magrì, C., Moretti, P., Schiavone, D., Tripaldi, S., 2008. Integrated geophysical approach for imaging the Porto Azzurro (Elba, Italy) plutons and the associated structures. In: Proceedings 33rd International Geological Congress, Oslo, 6–14 August 2008.

Smith, S.A.F., Holdsworth, R.E., Collettini, C., 2011. Interactions between low-angle normal faults and plutonism in the upper crust: Insights from the Island of Elba, Italy. GSA Bulletin 123 (1/2), 329–346. doi:10.1130/B30200.1.

Srivastava, D.C., Engelder, T., 1990. Crack-propagation sequence and pore fluid conditions during fault-bend folding in the Appalachian Valley and Ridge, central Pennsylvania. Geological Society of America Bulletin 102, 116–128.

Stearns, D.W., 1968. Certain aspects of fractures in naturally deformed rocks. In: Riecker, R.E. (Ed.), Rock mechanics seminar. Bedford. Terrestrial Sciences Laboratory, pp. 97–118.

Tanelli, G., 1983. Mineralizzazioni metallifere e minerogenesi della Toscana. Memorie della Società Geologica Italiana 25, 91–109.

Turcotte, D.L., Schubert, G., 2002. Geodynamics, Second Edition. Cambridge University Press, Cambridge, pp. 456.

Woodford, D.T., Sisson, V.B., Leeman, W.P., 2001. Boron metasomatism of the Alta stock contact aureole, Utah: evidence from borates, mineral chemistry and geochemistry. American Mineralogist 86, 513–533.